J. Fluid Mech. (2011), *vol.* 671, *pp.* 535–558. © Cambridge University Press 2011
doi:10.1017/S0022112010005872

Forced turbulent fountain flow behaviour

N. WILLIAMSON[1]†, S. W. ARMFIELD[1] AND WENXIAN LIN[2]

[1]School of Aerospace, Mechanical and Mechatronic Engineering, The University of Sydney, NSW 2006, Australia

[2]School of Engineering and Physical Sciences, James Cook University, Townsville, QLD 4811, Australia

(Received 3 June 2010; revised 19 October 2010; accepted 8 November 2010; first published online 8 February 2011)

Numerical simulations of turbulent fountain flow are used to investigate the important energy and mass transfer mechanisms present in the forced fountain flow regime, which has been reported to exist at Froude numbers (Fr) greater than 3. The flow is equivalent to a negatively buoyant jet with three flow streams, the inner upflow (IF), the outer downflow (OF) and the surrounding ambient fluid (AF). Simulation results are presented for $Fr = 4$ and 7 at Reynolds number $Re = 3350$. The mean fountain penetration height scales with the previously reported relation $Z_m/R_0 = 2.46Fr$, where R_0 is the source radius, but the assumptions behind analytical derivations of the relation are not supported by the present results. The results suggest that the OF may be relatively well described by the dynamics of a pure line plume surrounding the IF but with higher entrainment owing to the unsteady pulsing behaviour of the flow entering the OF from the IF. The length scale for a pure plume appears to apply at $Fr = 7$ in the OF and a degree of self-similarity exists. Comparisons with previous results suggest the IF is not fully developed at $Fr = 7$ and entrainment into the IF from the OF may not occur until $Fr > 15$.

Key words: jets, plumes/thermals

1. Introduction

In turbulent fountains or jets, where a buoyancy force opposes the initial fluid motion, the flow rises to its maximum height and stagnates before forming an outer downflow (OF) which interacts with the inner flow (IF) and the ambient fluid (AF), as illustrated by the schematic in figure 1. Fountain flows occur widely in industrial and geophysical flows but are also an example of the more general shear mixing flow, where the buoyancy force is aligned with the flow. Specific attention has been given to flow occurrences in air-conditioning and heating in large buildings (Baines, Turner & Campbell 1990; Lin & Linden 2005), volcanic eruptions (Kaminski, Tait & Carazzo 2005; Suzuki *et al.* 2005) and the dynamics of cumulus cloud tops (Turner 1966). Fully turbulent fountain flow is characterised only by the Froude number,

$$Fr = \left(\frac{M_0 W_0}{R_0 F_0}\right)^{1/2}, \tag{1.1}$$

† Email address for correspondence: n.williamson@usyd.edu.au

https://doi.org/10.1017/S0022112010005872 Published online by Cambridge University Press

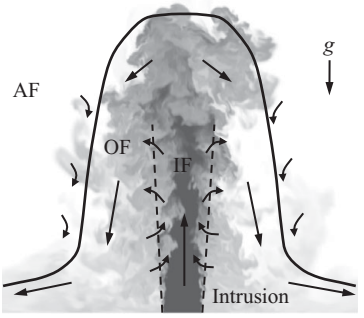


FIGURE 1. Schematic of turbulent fountain flow structure.

where R_0 is the radius of the source, and M_0 and F_0 are the source momentum flux and the buoyancy flux defined as

$$M_0 = \int_0^{R_0} 2\pi r \overline{U_{z,0}}^2 \,\mathrm{d}r, \quad F_0 = \int_0^{R_0} 2\pi\sigma r \overline{U_{z,0}} \,\mathrm{d}r, \tag{1.2}$$

where $\overline{U_{z,0}}$ is the time-averaged vertical velocity at the source, σ is the reduced gravity between the fountain source and the ambient fluid and is defined as $\sigma = g(\rho_0 - \rho_\infty)/\rho_\infty$, with the subscript 0 indicating the fountain source and ∞ the ambient fluid. The characteristic velocity is $W_0 = Q_0/A_0$, with Q_0 and A_0 being the volume flow rate of the fountain at the source and source cross-sectional area, respectively.

Kaye & Hunt (2006) found that the fountain behaviour can be classified into three distinct regimes, 'very weak flow' for $Fr \lesssim 1$, 'weak flow' for $1 \lesssim Fr \lesssim 3$ and 'forced flow' for $Fr \gtrsim 3$. The identification of these regimes and the corresponding scaling relations for the fountain steady-state penetration depth Z_m have been the subject of a number of studies (Turner 1966; Mizushina *et al.* 1982; Campbell & Turner 1989; Baines *et al.* 1990; Cresswell & Szczepura 1993; Zhang & Baddour 1997, 1998; Bloomfield & Kerr 2000; Lin & Armfield 2000*a*,*b*; Kaye & Hunt 2006; Williamson, Armfield & Lin 2008*a*; Williamson *et al.* 2008*b*; Baddour & Zhang 2009).

For turbulent very weak fountains, the momentum flux is relatively weak so the fountain rises to a small height, providing the pressure head to accelerate the flow radially giving, for round fountains, $Z_m/R_0 = C_1 Fr^{2/3}$ (Zhang & Baddour 1997, 1998; Lin & Armfield 2000*b*; Kaye & Hunt 2006; Williamson, Armfield & Lin 2010), where C_1 is a constant of proportionality. Williamson *et al.* (2010) showed that for $Fr \gtrsim 0.4$, the contribution of the source velocity head, Z'_m, becomes significant. The contribution of the velocity head to the penetration height leads to the following scaling $Z'_m \sim U_0^2/\sigma \equiv M_0^2/Q_0F_0$ or $Z'_m/R_0 \sim Fr^2$ (Zhang & Baddour 1997; Kaye & Hunt 2006; Williamson *et al.* 2010). In this way, over the range $0.4 \lesssim Fr \lesssim 3$, the flow has two components contributing to the fountain height so $Z_m/R_0 = C_1 Fr^{2/3} + C_2 Fr^2$, where C_2 is another constant. For $Fr \gtrsim 3$, the flow approaches a linear scaling $Z_m/R_0 = C_3 Fr$, where C_3 is a constant, or equivalently $Z_m \sim M_0^{3/4}/F_0^{1/2}$, as first identified by Turner (1966) using dimensional arguments and laboratory experiments. Further experiments by Baines *et al.* (1990) and Mizushina *et al.* (1982) show this relation holds up to at least $Fr \approx 300$. Numerous other experiments support the scaling but there is some variation in the constant with $C_3 = 2.1$–3.06 (Turner 1966; Campbell & Turner 1989; Baines *et al.* 1990; Cresswell & Szczepura 1993; Kaye & Hunt 2006; Williamson *et al.* 2008*b*; Baddour & Zhang 2009).

https://doi.org/10.1017/S0022112010005872 Published online by Cambridge University Press

Early experimental studies provide some details of the structure of the flow in the high-Froude-number regime. Mizushina *et al.* (1982) used anemometer probes to measure point velocity and temperature for fountain flow with $Fr \approx 5$–260 and Cresswell & Szczepura (1993) used laser Doppler anemometry and fast themocouples to measure turbulent quantities in an $Fr = 3.16$ flow with a hot water jet directed downwards. Other studies include those of Sendan, Behnia & Abreu (1978) who provide temperature measurements only and Demetriou (1978). Mizushina *et al.* (1982) showed that unlike plumes or non-buoyant jets, in fountain flow, both the upflow and downflow continue to develop along their trajectories so the flow never attains self-similarity and the flow statistics vary with axial location and Froude number.

Using the integral model that Morton (1959) had developed for plumes, Abraham (1967) obtained analytically the linear high-Froude-number scaling. Kaye & Hunt (2006) later obtained the same result with a similar approach by assuming entrainment in high-Froude-number forced fountains to be similar to that in non-buoyant jets. In both studies, only the initial upflow was considered, where the OF had not formed. Turner (1966) provided an empirical connection between the initial flow and the final established flow which shows that the initial maximum height (Z_M) reached by a vertical turbulent fountain is related to the final mean height by $Z_M \approx 1.43 Z_m$ (Kaye & Hunt 2006). Other modelling attempts include the work of Bloomfield & Kerr (1998, 2000) and Lin & Linden (2005). Bloomfield & Kerr (2000) extended the integral model of Morton (1959) to a fully established fountain flow by modifying the entrainment mechanism to include radial entrainment velocity ω from the IF into the OF (ω_β), the OF into the IF (ω_α) and the AF into the OF (ω_γ). The authors suggested two formulations for these entrainment processes. The most successful of these was the assumption that ω_α depends on the IF vertical velocity so $\omega_\alpha = \alpha W_{IF}$, where W_{IF} is the bulk IF vertical velocity. ω_β and ω_γ were assumed to depend on the OF vertical velocity only. The corresponding entrainment coefficients for these flow streams, α, β, γ, were taken to be constant with height and Froude number. In testing the model, they took $\alpha = 0.085$, based on earlier experiments of the initial rise of turbulent fountain flow in Bloomfield & Kerr (1998). The coefficients γ and β were taken to be 0.147, a typical value for entrainment in a pure line plume. Results obtained by numerical integration of the equations compared well with the quantities available in Mizushina *et al.* (1982), including the fountain width, velocity in both streams and upflow buoyancy. The model was sensitive to the value of γ.

The apparent success of the Bloomfield & Kerr (2000) approach suggests that the behaviour of the OF and the IF are essentially de-coupled and can be treated as two separate well-understood flows, a plume and a jet. Kaye & Hunt (2006) also support this idea in that they only consider the upflow, in the limit of a very high-Froude-number flow, which they take to behave like a turbulent jet. The proof of this concept in their work is that they obtained the established linear Froude number scaling using this model. Understanding the mixing behaviour and the dynamics of the two streams (IF and OF) is critical for successful development of scaling models in more complex ambient environments. Measurements required to understand this behaviour are not currently available in the literature and most models are validated by comparing the fountain penetration height only. The objective of this work is to provide details of the flow behaviour in the forced flow regime and the mass and momentum exchanges between the IF, OF and AF. To this end, direct numerical simulations have been obtained for turbulent fountain flow at $Fr = 4$ and 7 and the results have been analysed. While the paper does not focus specifically on fountain applications in this range of Froude numbers, there are many examples of such flows.

https://doi.org/10.1017/S0022112010005872 Published online by Cambridge University Press

For instance, in heating, ventilation and cooling applications, a vent length scale of 0.15 m, velocity of 1.5 m s^{-1} and temperature variation of 15 °C gives $Fr = 5.45$. Such flows will occur as fountains in heating from ceiling vents such as are used in large auditoriums and cooling from floor vents in displacement cooling. Similarly, effluent discharge flows can have Froude numbers in the range we have investigated.

Our numerical model is described in § 2. In § 3, the general flow behaviour is described and the rise time and penetration height scaling results are presented. In § 4, an analysis of the entrainment behaviour and the momentum transfers is presented with reference to prior modelling and scaling results. The conclusions are presented in § 6.

2. Numerical formulation

We use direct numerical simulation (DNS) to solve the Navier–Stokes equations for incompressible flow and employ the Boussinesq approximation. The non-dimensionalised continuity, momentum and scalar transport equations are:

$$\frac{\partial u_i}{\partial x_i} = 0, \tag{2.1}$$

$$\frac{\partial u_i}{\partial t} + \frac{\partial (u_i u_j)}{\partial x_j} = -\frac{\partial p}{\partial x_i} + \frac{1}{Re}\frac{\partial^2 u_i}{\partial x_j \partial x_j} - \frac{\phi}{Fr_0^2}, \tag{2.2}$$

$$\frac{\partial \phi}{\partial t} + \frac{\partial (u_j \phi)}{\partial x_j} = \frac{1}{RePr}\frac{\partial^2 \phi}{\partial x_j \partial x_j}, \tag{2.3}$$

where $Pr = \nu/\alpha$ is the Prandtl number, the Reynolds number is defined as $Re = W_0 R_0/\nu$ and ν and α are the kinematic viscosity and scalar diffusivity of the fluid, respectively. The velocity (U_i), temperature (θ), pressure (P), time (T) and length (X_i) turn non-dimensional as $u_i = U_i/W_0$, $\phi = (\theta - \theta_\infty)/(\theta_0 - \theta_\infty)$, $p = P/\rho W_0^2$, $t = T W_0/R_0$ and $x_i = X_i/R_0$, respectively.

The discretised governing equations were solved in finite-volume form on a non-staggered Cartesian grid. The spatial derivatives were discretised using second-order central finite differences except for the scalar advective term which is nominally a second-order centred scheme but with the ULTRA-flux limiter of Leonard & Mokhtari (1990) applied. The advective terms were advanced in time using the second-order Adams–Bashforth scheme while the viscous terms were advanced using the Crank–Nicolson scheme. Rhei–Chow interpolation was used for the cell face velocities in the pressure solver. The system of equations was solved with the BICGSTAB solver with a Multi-grid Jacobi pre-conditioner. The computational domain is a rectangular box in which the top and sidewalls are open boundaries. The open boundaries have a zero-gradient condition on the velocity and scalar field and zero second derivative on the pressure correction term. The bottom boundary is no-slip/adiabatic, except for the fountain source located in the centre where the normal velocity and temperature have uniform profiles at W_0 and ϕ_0.

We present results for high-Froud-number flows $Fr = 4$ and 7 at $Re = U_0 R_0/\nu = 3350$ with $Pr = 7$. The details of the simulation parameters are given in table 1. We also refer to a previous $Fr = 2.1$ simulation presented in Williamson *et al.* (2008*a*, 2010).

A regular Cartesian grid is used which is uniform in the horizontal x, y plane within a distance $Lu_{x,y}$ of the centre of the source. Outside this region, the grid is stretched at approximately 5 % growth rate. The grid is uniform in the axial direction up to

https://doi.org/10.1017/S0022112010005872 Published online by Cambridge University Press

Fr	Pr	Re	Δx, y, Δz	$L_{x,y}$,L_z	$N_{x,y}$,N_z	$Lu_{x,y}$,Lu_z
4.0	7.0	3350	0.03,0.06	16,17	293,197	3,9.5
7.0	7.0	3350	0.031,0.06	20,32	325,325	3.5,17

TABLE 1. Simulation parameters Δx, y, z, $L_{x,y,z}$ and $N_{x,y,z}$ give the non-dimensional grid size at the source, the domain size and the number of nodes, respectively.

Lu_z and stretched at 3 % thereafter. For the $Fr = 4$ and $Fr = 7$ simulations, the source is prescribed as a uniform steady inlet profile, while the $Fr = 2.1$ simulation has an unsteady turbulent inlet velocity profile obtained by performing a separate periodic pipe flow simulation. The details of this work are given in Williamson *et al.* (2010). The ratio of grid cell size (ΔX, ΔY, ΔZ) to Kolmogorov scale (η) ranges from 1 to 3.5. The smallest scalar turbulent length scale, $\eta_\phi = \eta/\sqrt{Pr}$, so DNS spatial resolution requirements are not met here with a Prandtl number of 7. The application of the flux limiter to the advective term provides sufficient damping and prevents non-physical negative temperatures from occurring in the present simulations and was not found to be problematic to the solution in Williamson *et al.* (2010).

3. General results and flow observations

The flow development of the $Fr = 4$ and $Fr = 7$ simulations is shown in figures 2 and 3 with contours of ϕ. In both cases, the initial transient flow features are interesting. The initial startup flow consists of the rising collimated IF stream with a vortex ring rising with the front of the IF. When the fountain reaches its initial maximum height, the ring rises off the top and sheds dense fluid. At $Fr = 4$, the vortex ring detaches from the upflowing fountain but is overcome by buoyancy forces and descends back to the source. At $Fr = 7$, the weaker buoyancy forces allow the structure to rise further and escape the computational domain. With a bigger domain, the vortex would presumably eventually dissipate and have the same behaviour as at $Fr = 4$. At $Fr = 2.1$, the ring does not detach from the initial upflow (Williamson *et al.* 2008*a*, 2010). On reaching the maximum initial height, the flow reverses and the OF is established followed by the intrusion along the bounding lower wall. The behaviour of the vortex head has been examined for weak fountain flow by Marugán-Cruz, Rodríguez-Rodríguez & Martínez-Bazán (2009), with $Fr \approx 0.3$–1.9, where the head does not detach. After reaching its maximum initial height, the OF forms and the overall fountain height decreases. The fountain then fluctuates about its mean height with none of the instability observed in laminar flow (Williamson *et al.* 2008*b*). This behaviour is illustrated in supplementary movies 1 and 2 (available at journals.cambridge.org/flm).

The structure of the fully developed flow is illustrated in figure 4 for $Fr = 2.1$ and 4 and in figure 5 for $Fr = 7$ with velocity vectors, pressure contours and shading indicating ϕ. In all the simulations, there is a high-pressure region where the intrusion forms and the OF meets the bounding wall. For $Fr = 2.1$ and 4.0, the IF is relatively unmixed with ambient fluid. At $Fr = 7$ for $z < 10$, the IF has a potential core with mixing in a shear layer between the IF and OF. Vortex structures move through the shear layer both up and down the fountain. The low-pressure regions and circulations indicated by the vectors indicate where vortex structures exist in the instantaneous flow in figure 5. The interaction of the upflow and downflow generates high- and low-pressure regions forcing the flow to bend in a sinuous way, similar to the helical

https://doi.org/10.1017/S0022112010005872 Published online by Cambridge University Press

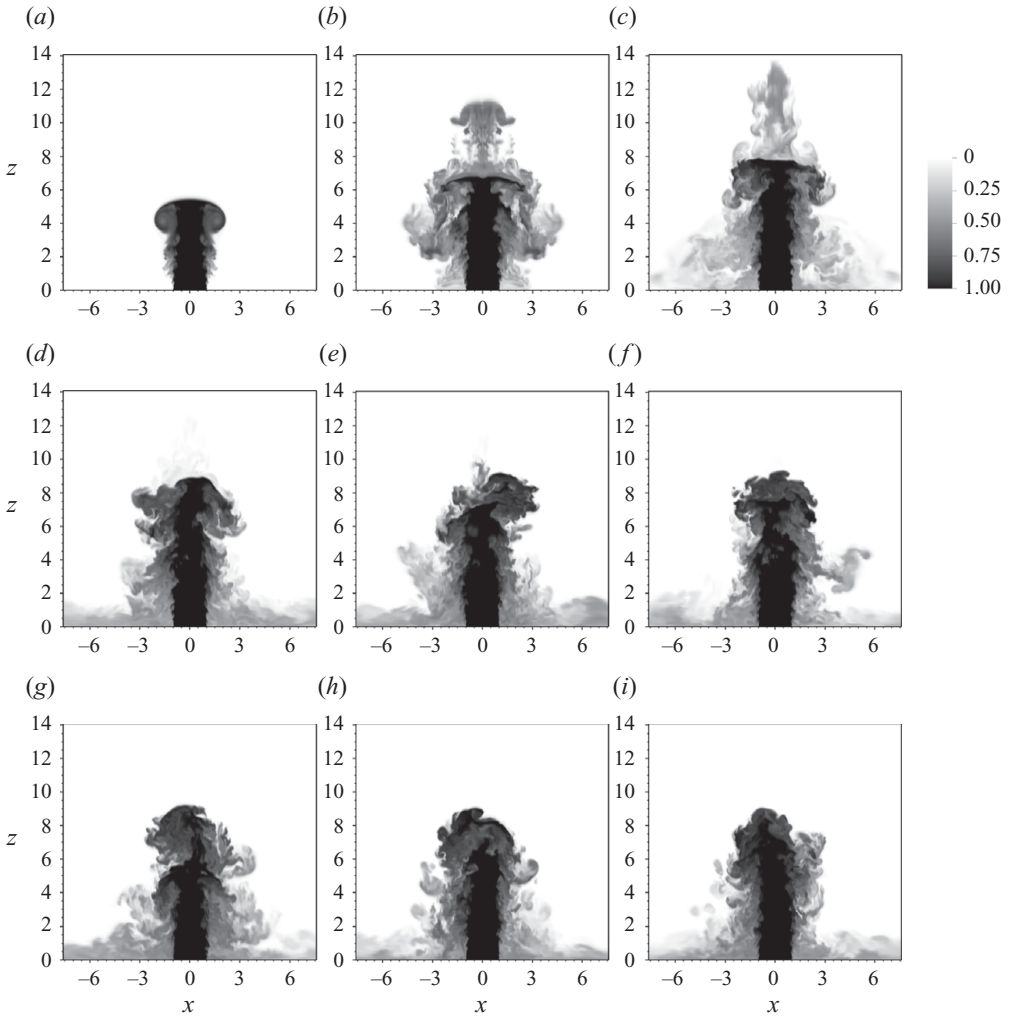


FIGURE 2. Flow development of $Fr = 4$ simulation from $t = 12.0$ (a) in increments of $\Delta t = 24.5$. Shading indicates ϕ with the scale given above.

instability observed in turbulent jets. This occurs both in the potential core and in the head of the fountain. At $z \approx 10$, this sinuous flapping behaviour is very strong. At the top of the fountain, referred to hereafter as the cap region, the flow is highly unsteady. Here, a vortex ring forms around rising pulses in the IF and is then shed into the downflow. The ejection and re-entrainment of fluid here is complex. The behaviour is approximately periodic with the period of oscillation $t \approx 37$.

In the $Fr = 2.1$, 4 and 7 simulations, fluid is expelled from the cap region in either antisymmetric pulses down one side or in non-uniform annular ejections out of the cap region. The vortex ring continually collapses and reforms with this oscillation. At $Fr = 2.1$ and $Fr = 4$, the IF and cap region are more stable than at $Fr = 7$.

The time trace of the source pressure and the maximum penetration height is given in figure 6. The source pressure is given as this is an important quantity for low-Froude -number flow (Williamson *et al.* 2010). The rise time of high-Froude-number turbulent fountains was shown to scale as $t_m \sim Fr^2$ empirically by Pantzlaff &

https://doi.org/10.1017/S0022112010005872 Published online by Cambridge University Press

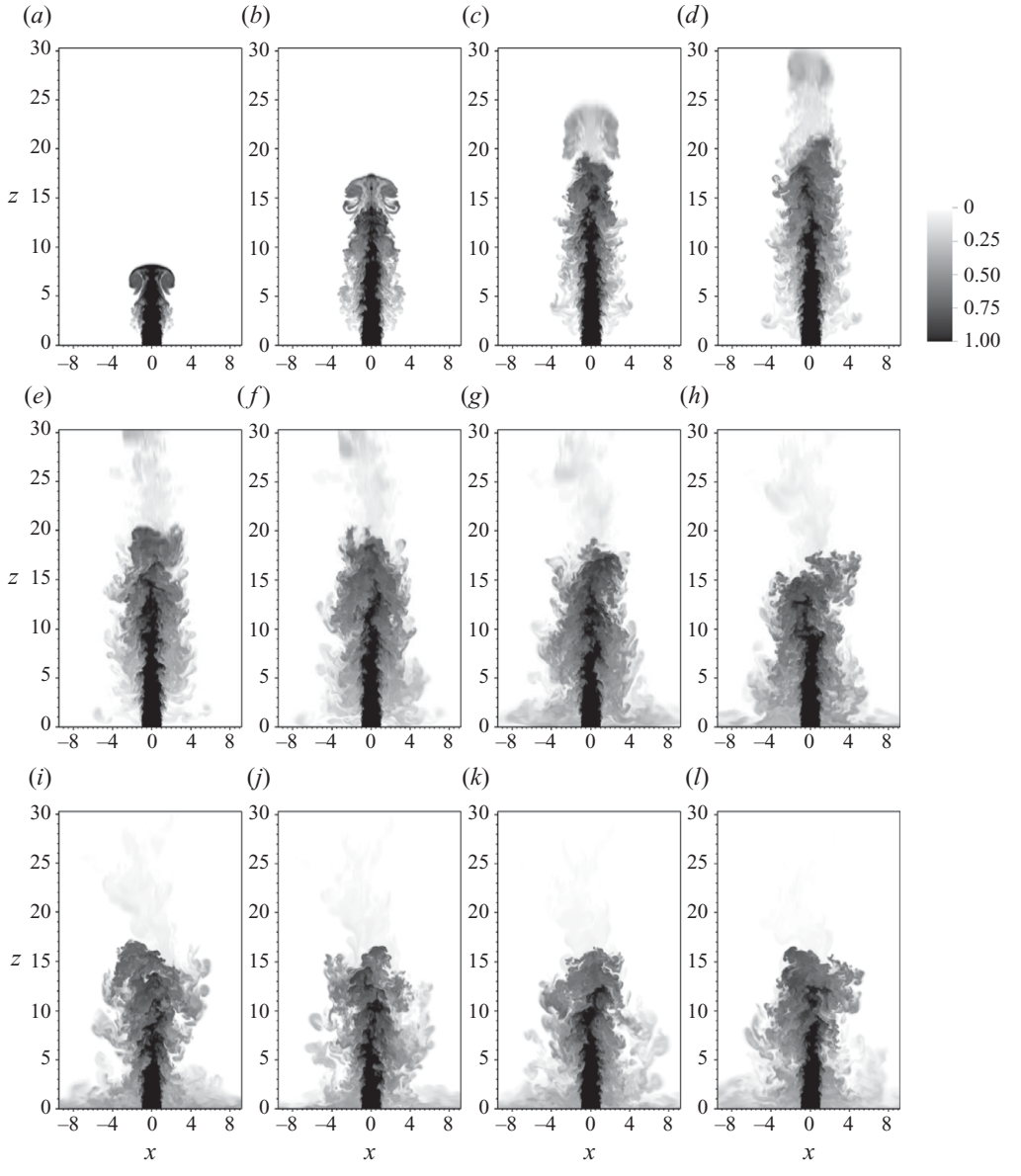


FIGURE 3. Flow development of $Fr = 7$ simulation from $t = 16.7$ (a) in increments of $\Delta t = 24.5$. Shading indicates ϕ with the scale given above.

Lueptow (1999) and then experimentally by Williamson *et al.* (2008*b*) for laminar high-Froude-number fountain flow. This scaling does not collapse the $Fr = 4$ and $Fr = 7$ curves in figure 6, possibly because the flow regime is close to the transition point, so the time axis of figure 6 is unscaled.

The source pressure is initially negative as the annular vortex at the head of the fountain forms and rises above the source. The pressure then rises slightly and is nearly constant until the downflow meets the bounding wall and the intrusion forms. At $Fr = 4$, the pressure rises over $t = 25$–80 before reaching an approximately constant steady value. The fountain height rises over $t = 0$–35. At $t \approx 35$, the vortex ring detaches and continues to rise while the fountain height decreases slightly. The

https://doi.org/10.1017/S0022112010005872 Published online by Cambridge University Press

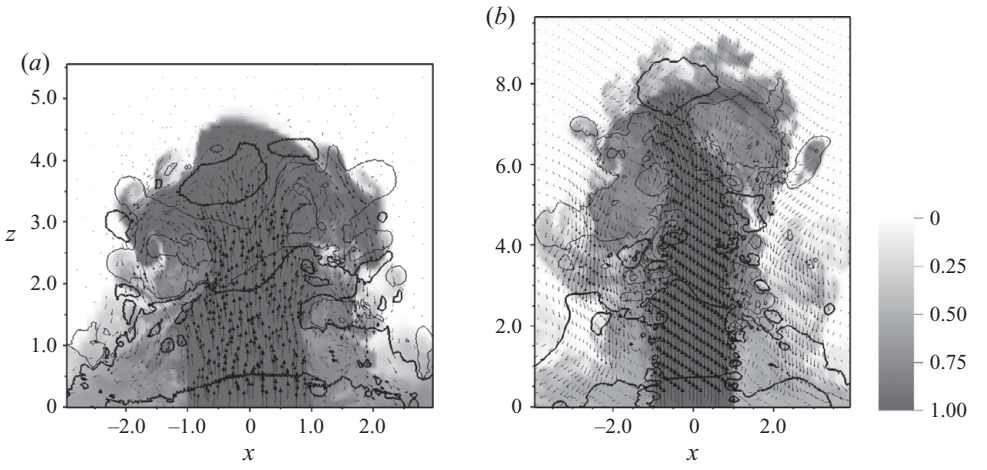


FIGURE 4. Fully developed flow structure of $Fr = 2.1$ flow at $t = 36$ (a) and $Fr = 4$ flow at $t = 174$ (b). Shading indicates ϕ with scale given above and velocity vectors are scaled to give relative velocity magnitude. Thick lines indicate p contours of 0.03 and 0.25 in (a); 0.1 and 0.02 in (b). Thin lines give p contours of -0.25 and -0.03 in (a); -0.1 and -0.02 in (b).

vortex ring stagnates and then falls downwards meeting the fountain top at $t \approx 85$. The maximum location at $r = 0$, where $\phi = 0.1$, gives the approximate location of the top of the detached vortex while the minimum location of $\phi = 0.1$ gives approximately the top of the fountain. The fountain reaches steady-state behaviour at approximately $t \approx 120$ and flow statistics have been taken over $t \approx 120$–240. For $Fr = 7$, the vortex ring separates at $t \approx 65$, as shown in figure 3(c). Most of the vortex leaves the top of the domain, with some of the fluid falling backwards to the source, meeting the fountain at $t \approx 200$. Flow statistics have been taken over $t \approx 200$–310. The source pressure is steady until $t \approx 80$ when it rises as the intrusion forms over the period $t \approx 80$–150, and is steady thereafter.

In figure 7, the fountain mean penetration height, defined as the point where $\overline{u_z} = 0$, is plotted against the Froude number together with the other published results for this range of Froude numbers. There is a high degree of correspondence between the high-Reynolds-number simulations in this study and the previous results. From $Fr = 2.1$ to 7, the height moves towards the $z_m = 2.46Fr$ line. The point where the flow can be considered fully forced is not clear from the figure. Zhang & Baddour (1998) performed experiments with round saline/fresh water fountains over the range $850 < Re < 12\,750$ and $0.37 < Fr < 36.2$ and found for $Fr > 7$ the mean maximum penetration height follows $z_{\max} = 3.06Fr$ but for $Fr < 7$ is better represented by $z_{\max} = 1.7Fr^{1.3}$. Cresswell & Szczepura (1993) demonstrated that at $Fr = 3.16$, the upflow is dominated by the potential core which extends to $z = 4$ where it meets the cap region while Kaye & Hunt (2006) suggests that the weak-forced transition is at $Fr = 3$. This suggests that the fountain penetration height may follow the linear Froude number scaling before the flow is fully forced as would be defined by the physics of the mixing and entrainment in the structure.

4. Discussion

In this section, details of the mass and momentum transfers in the flow are analysed with the goal of understanding the mechanisms which lead to the behaviour observed

https://doi.org/10.1017/S0022112010005872 Published online by Cambridge University Press

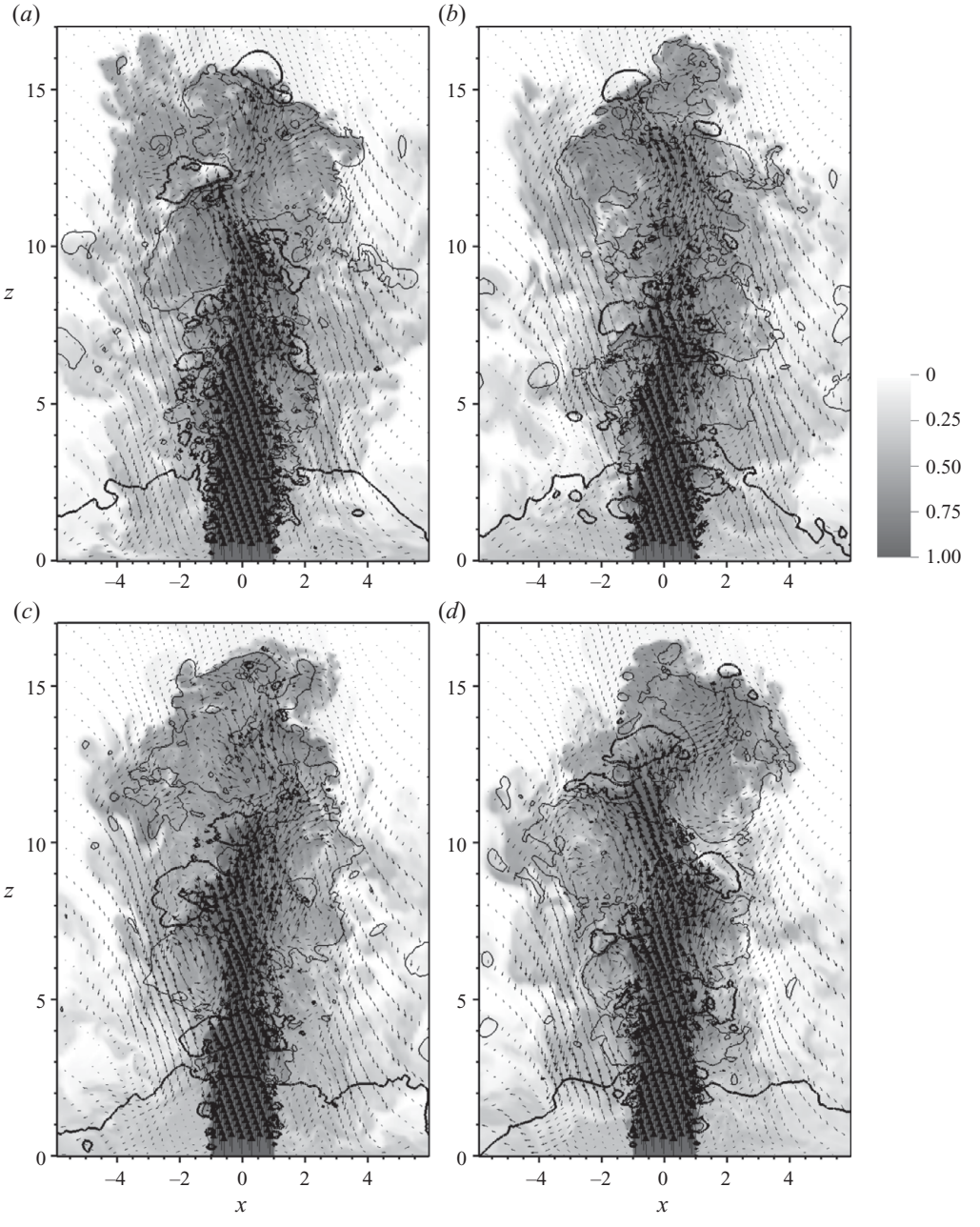


FIGURE 5. Fully developed flow structure of $Fr = 7$ simulation from $t = 228$ (a) in increments of $t = 14.7$ (b–d). Shading indicates ϕ with scale given above. Thick lines give $p = 0.015$ contours, thin lines give $p = -0.015$ contours.

in § 3. The flow field has been interpolated onto a cylindrical coordinate system (r, z, θ). Unless otherwise stated, the statistics presented in this work are normalised by source variables, as shown in § 2. Other choices would be the local centreline velocity or the local mean difference between the upflow and downflow, but since

https://doi.org/10.1017/S0022112010005872 Published online by Cambridge University Press

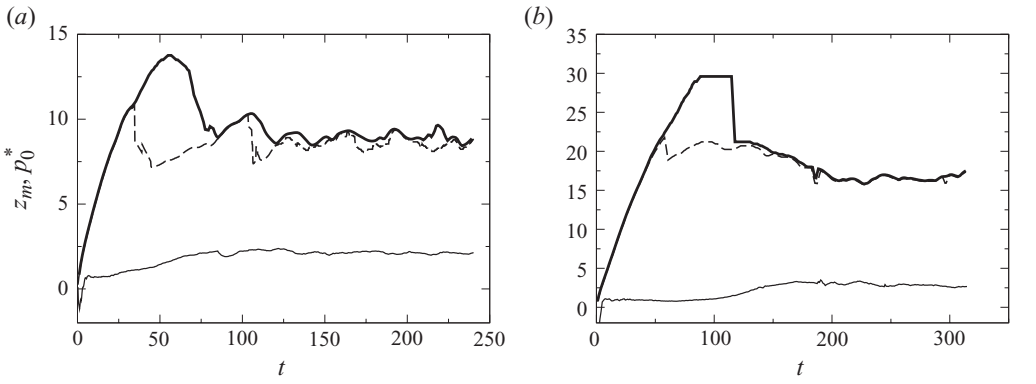


FIGURE 6. Time evolution of fountain height at $r = 0$ and normalised source pressure head $p_0^* = p_0 Fr^2$, at $r = 0$ and $z = 0$ for (*a*) $Fr = 4$ and (*b*) $Fr = 7$. $p_0^*(t)$ is indicated by thin solid lines. The thick solid line indicates the maximum location of $\phi = 0.1$, which gives the approximate location of the top of the detached vortex. The dashed line indicates minimum location of $\phi = 0.1$ which gives the approximate location of the fountain height $z_m(t)$.

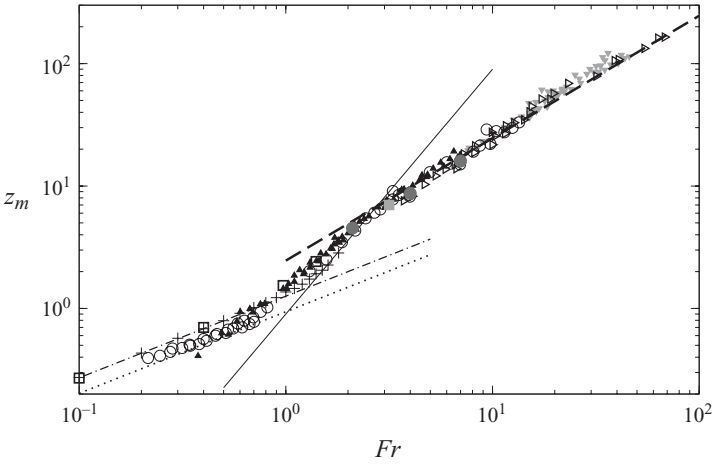


FIGURE 7. Normalised fountain penetration height with Froude number where the dash-dotted line is $1.26Fr^{2/3}$ (Lin & Armfield 2000*b*), the dotted line $0.94Fr^{2/3}$ (Kaye & Hunt 2006), the solid line $0.9Fr^2$ (Kaye & Hunt 2006) and the dashed line $2.46Fr$ (Turner 1966). Data symbols indicate: ○, Kaye & Hunt (2006); +, Lin & Armfield (2000*a*) (uniform source velocity profile); ▲, Zhang & Baddour (1998); ■, Cresswell & Szczepura (1993); ▼, Baddour & Zhang (2009); ▷, Papanicolaou & Kokkalis (2008); □, Williamson *et al.* (2010); and ● are present simulations ($Fr = 4$ and 7) and Williamson *et al.* (2008*b*, 2010) ($Fr = 2.1$).

at these Froude numbers the flow is developing over most of its height and is not self-similar, the inlet condition is a better choice.

The vertical profiles of the Reynolds stresses and mean flow quanitites, obtained by time and azimuthal averaging, are given in figure 8 at $r = 0$. In both $Fr = 4$ and $Fr = 7$, the centreline value of $\overline{\phi}$ is constant until $z = 5$. Thereafter $\overline{\phi}$ drops nearly linearly from $z = 5$ to $z = 8$ for $Fr = 4$ and $z = 5$ to $z = 15$ for $Fr = 7$, and then drops rapidly to zero. At $Fr = 4$, the centreline velocity decreases nonlinearly over $z \approx 0$–6 and then linearly over $z \approx 6 - z_m$, where z_m is the maximum non-dimensional penetration height defined as the point where $\overline{u_z} = 0$. At $Fr = 7$, the centreline velocity appears to

https://doi.org/10.1017/S0022112010005872 Published online by Cambridge University Press

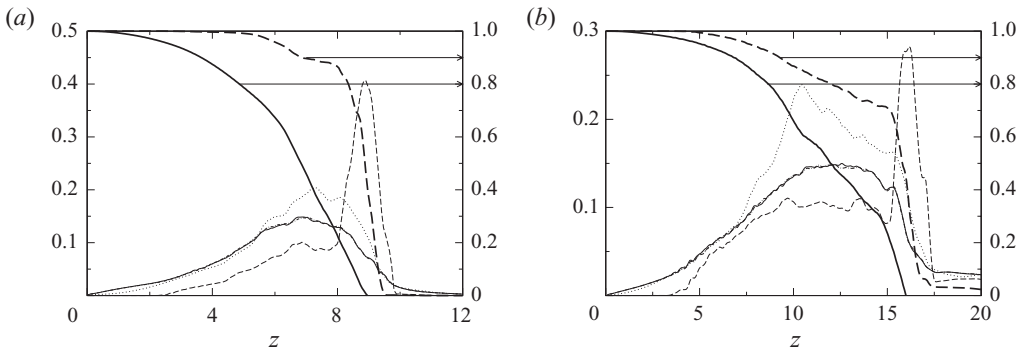


FIGURE 8. $\overline{u_z'u_z'}^{0.5}$ – dotted line, $\overline{u_r'u_r'}^{0.5}$ – thin solid line, $\overline{u_\theta'u_\theta'}^{0.5}$ – dash-dotted line, $\overline{\phi'\phi'}^{0.5}$ – dashed line, $\overline{u_z}$ – thick line, $\overline{\phi}$ – thick dashed line for $Fr = 4$ (*a*) and $Fr = 7$ (*b*), all interpolated onto $r = 0$.

decrease with three behaviours. Over $z \approx 0$–9, the velocity decreases nonlinearly, over $z \approx 9$–15 the decrease is nearly linear and over $z \approx 15 - z_m$ the velocity also decreases linearly but at a faster rate. This is discussed further in § 4.1.

At $Fr = 4$, in figure 8(*a*), the Reynolds stresses and $\overline{\phi'\phi'}^{0.5}$ peak first at $z \approx 6.8$ where the large eddy structures from the downflow and cap region penetrate the inner flow stream advecting downflow fluid into the upflow. At $z = z_m$, intermittency in the location of the interface causes a spike in $\overline{\phi'\phi'}^{0.5}$.

At $Fr = 7$, in figure 8(*b*), $\overline{u_z'u_z'}^{0.5}$ peaks at $z = 10$ and then declines towards $z = z_m$. The scalar fluctuations $\overline{\phi'\phi'}^{0.5}$ and $\overline{u_r'u_r'}^{0.5}$, $\overline{u_\theta'u_\theta'}^{0.5}$ are nearly constant in magnitude for $z = 10 - z_m$, while $\overline{u_z'u_z'}^{0.5}$ decreases more slowly than $\overline{u_z}$. At $z = z_m$, $\overline{\phi'\phi'}^{0.5}$ peaks with flow intermittency and the Reynolds stresses are non-zero until above $z \approx 20$. The ratio of $\overline{u_z'u_z'}^{0.5}/\overline{u_z}$ increases with height for both $Fr = 4$ and $Fr = 7$.

The radial profiles of $\overline{u_z}$, $\overline{u_r}$ and $\overline{\phi}$ are given at different axial locations in figure 9(*a–d*) for $Fr = 4$ and in figure 10(*a–f*) for $Fr = 7$. The Reynolds stresses are given in figure 9(*e–h*) for $Fr = 4$ and in figure 11 for $Fr = 7$. The flow development observed here is generally similar to that observed in the initial region of a free jet (Boguslawski & Popiel 1979) but there are some key differences.

In a non-buoyant jet flow, the potential core ends at approximately 10–16R_0, (Mi, Nobes & Nathan 2001) but in both the fountain simulations, this distance is reduced. At $Fr = 4$, $\overline{u_z'u_z'}^{0.5}$ does not peak at the centreline until after $z = 8$, where the flow is affected by the cap region indicating the flow does not develop fully. At $Fr = 7$, $\overline{u_z'u_z'}^{0.5}$ peaks at the centreline at $z = 10.5$ where the shear layers merge and indicates the end of the potential core. Above $z = 10.5$, $\overline{u_z'u_z'}^{0.5}$ declines similarly to a non-bouyant jet (Boguslawski & Popiel 1979).

There is a double peak in the radial profile of $\overline{\phi'\phi'}^{0.5}$ below $z = 10.5$ for $Fr = 7$ and below $z = 4.5$ for $Fr = 4$. The inner peak occurs in the developing IF where there is a strong radial gradient in ϕ between the unmixed IF fluid and the OF fluid. This peak vanishes above the point where the shear layer merges. The larger second peak occurs in the region between the OF and the AF where intermittency in the location of this boundary and unsteady ejection of fluid from the top of the fountain increase the magnitude of this term.

https://doi.org/10.1017/S0022112010005872 Published online by Cambridge University Press

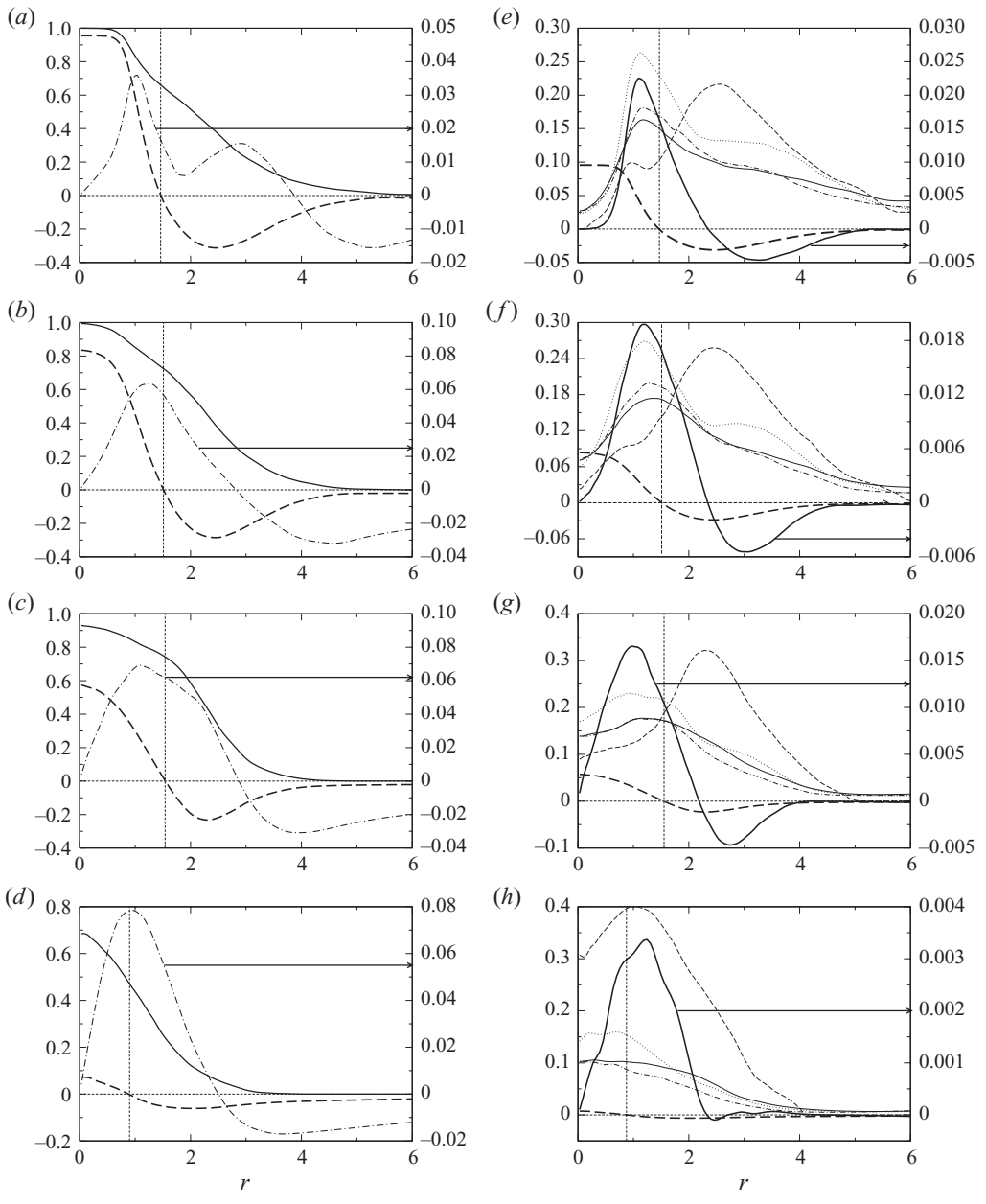


FIGURE 9. $Fr = 4$ radial profiles of: $(a–d)$ $\overline{u_z}$ – thick dashed line, $\overline{u_r}$ – dash-dotted line, $\overline{\phi}$ – solid line; $(e–h)$ $\overline{u_z' u_z'}^{0.5}$ – dotted line, $\overline{u_r' u_r'}^{0.5}$ – thin solid line, $\overline{u_\theta' u_\theta'}^{0.5}$ – dash-dotted line, $\overline{u_r' u_z'}^{0.5}$ – thick line, $\overline{\phi'\phi'}^{0.5}$ – dashed line, $0.1\overline{u_z}$ – thick dashed line. Plots are given at $z = 2.5$ (a,e), $z = 4.5$ (b,f), $z = 6.5$ (c,g), $z = 8.5$ (d,h). Straight thin dashed lines indicate IF/OF boundary and x-axis.

The quantities $\overline{u_r' u_r'}^{0.5}$ and $\overline{u_\theta' u_\theta'}^{0.5}$ are approximately equal at most locations in both simulations, similar to the behaviour of a non–buoyant jet. $\overline{u_r}$, which indicates local entrainment, is very small compared to $\overline{u_z}$ except near z_m. At $Fr = 7$, the peak in $\overline{u_r}$ moves further into the OF with increasing height. The large peak in $\overline{u_r}$ at $r = 5$

https://doi.org/10.1017/S0022112010005872 Published online by Cambridge University Press

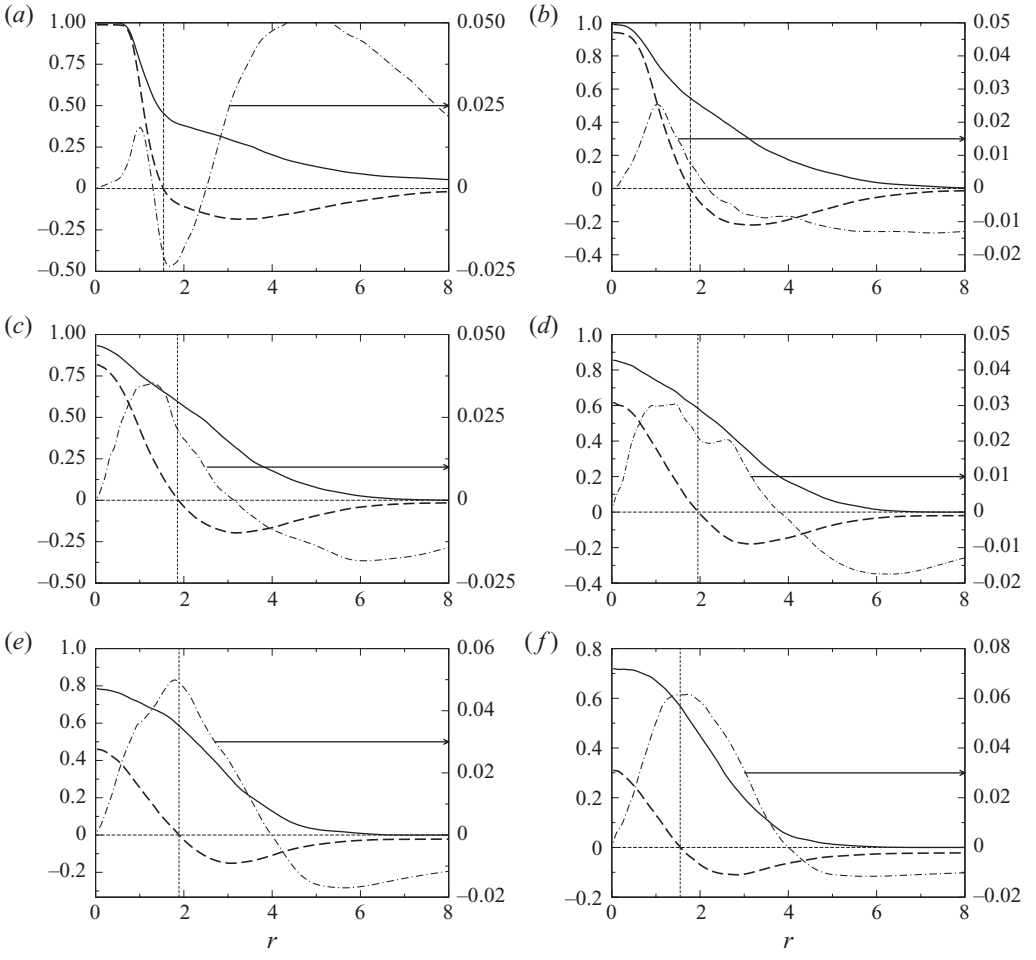


FIGURE 10. $Fr = 7$ radial profiles of $\overline{u_z}$ – thick dashed line, $\overline{u_r}$ – dash-dotted line, $\overline{\phi}$ – solid line. Plots are given at $z = 2.5$ (*a*), $z = 5.5$ (*b*), $z = 8.5$ (*c*), $z = 10.5$ (*d*), $z = 12.5$ (*e*) and $z = 14.5$ (*f*). Straight thin dashed lines indicate IF/OF boundary and x-axis.

and $z = 2.5$, shown in figure 10(*a*), is a result of the intrusion outflow. The radial location, r_d, where the maximum downward velocity in the OF occurs, is indicated in figure 12. In this figure and in figures 9–11, it is clear that for $r > r_d$ the OF expands freely outward into the ambient fluid but for $r < r_d$, the OF is confined by the IF and cannot expand inwards.

In figure 11, it is seen that the turbulent shear stress $\overline{u_r' u_z'}$ declines more rapidly than the normal Reynolds stresses over $z = 10.5 - z_m$, suggesting a reduction in shear production occurring between the IF and OF near the top of the fountain.

The results in figures 9–11 clarify that the flow is developing over most of the height. At $Fr = 4$, the potential core does not end before the top of the fountain. At $Fr = 7$, the potential core occupies most of the fountain height and the region above this is increasingly affected by radial flow into the OF and the changed dynamics of the cap region. This change in behaviour precludes the possibility of flow similarity in the IF and mixing region. The behaviour in the OF and the possibility of flow similarity therein is examined in § 4.1.

https://doi.org/10.1017/S0022112010005872 Published online by Cambridge University Press

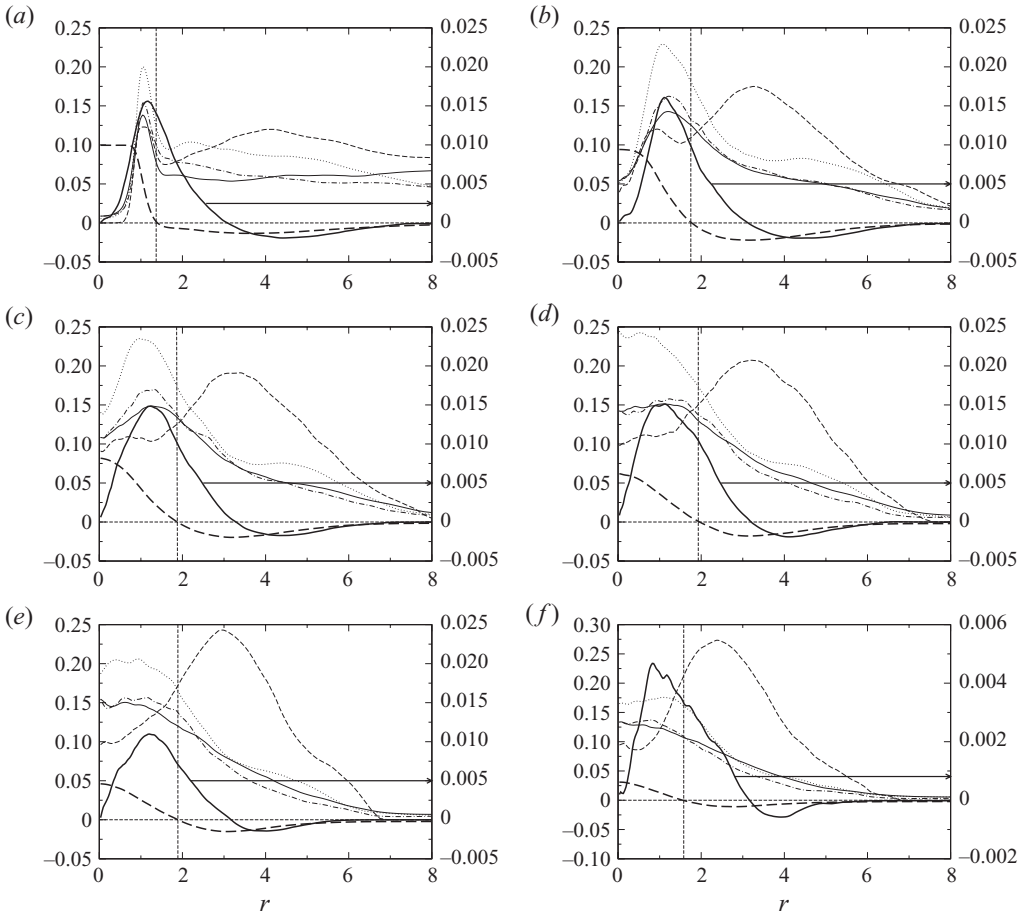


FIGURE 11. $Fr = 7$ radial profiles of $\overline{u_z'u_z'}^{0.5}$ – dotted line, $\overline{u_r'u_r'}^{0.5}$ – thin solid line, $\overline{u_\theta'u_\theta'}^{0.5}$ – dash-dotted line, $\overline{u_r'u_z'}^{0.5}$ – thick line, $\overline{\phi'\phi'}^{0.5}$ – dashed line, $0.1\overline{u_z}$ – thick dashed line. Plots are at $z = 2.5$ (a), $z = 5.5$ (b), $z = 8.5$ (c), $z = 10.5$ (d), $z = 12.5$ (e) and $z = 14.5$ (f). Straight thin dashed lines indicate IF/OF boundary and x-axis.

4.1. *Entrainment*

The fountain streams have been identified in figures 12(a) and 12(b) for $Fr = 4$ and $Fr = 7$, respectively. The IF/OF boundary, r_{io}, is defined as the radial location where $\overline{u_z} = 0$. The best definition of the boundary between the OF/AF, r_{oa}, is less clear. In an ideal pure plume, ru_r is a constant and the plume width B is usually obtained from $\sqrt{(b^2W)^2/(b^2W^2)}$, where

$$b^2W = 2\int_{r_1=0}^{r_2=\infty} \overline{u_z} r \, \mathrm{d}r, \tag{4.1}$$

$$b^2W^2 = 2\int_{r_1=0}^{r_2=\infty} \overline{u_z}^2 r \, \mathrm{d}r. \tag{4.2}$$

The equivalent length scale for a fountain OF half-width is,

$$B_{1/2} = \left(\left(2\int_{r_d}^{r_{lim}} \overline{u_z} r \, \mathrm{d}r \right)^2 \Big/ \left(2\int_{r_d}^{r_{lim}} \overline{u_z}^2 r \, \mathrm{d}r \right) + r_d^2 \right)^{1/2} - r_d. \tag{4.3}$$

https://doi.org/10.1017/S0022112010005872 Published online by Cambridge University Press

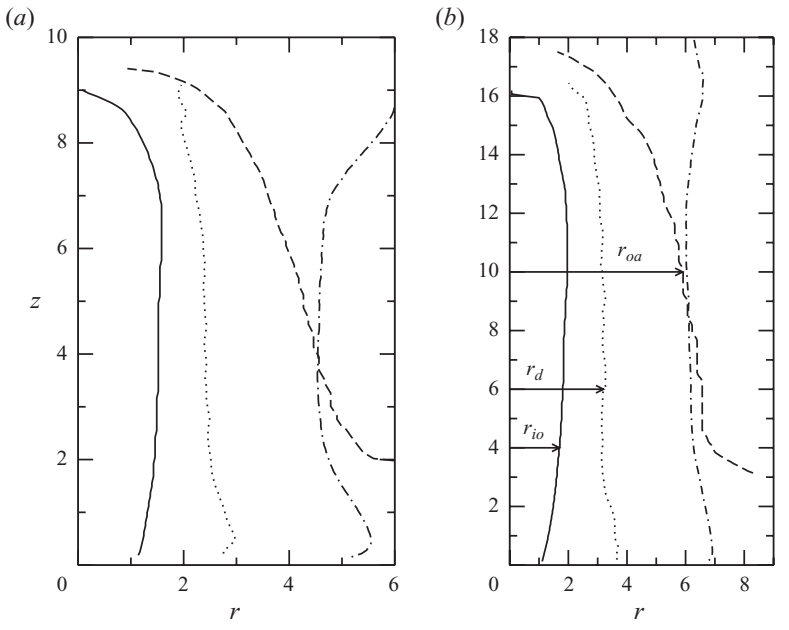


FIGURE 12. Boundaries between flow streams in $Fr = 4$ (a) and $Fr = 7$ (b). The solid line gives the IF/OF boundary, where $\overline{u_z} = 0$, the dotted line indicates $r_d(z)$, the dashed line gives r_{oa} where $\overline{\phi} = 0.025$ and the dashed-dotted line indicates r_{oa} defined by $B_{1/2} + r_d$.

The simulated domain is finite, so the integrals in (4.3) are evaluated to the edge of the domain $r = r_{lim}$. Over most of the fountain height, (4.3) is not very sensitive to the value of r_{lim}. The total distance from the centreline is $r_{oa} = B_{1/2} + r_d$. This definition of r_{oa} is plotted in figure 12. A second definition, defined as the location where $\phi = 0.025$, is also given in figure 12. The value $\phi = 0.025$ is arbitrary and it will be shown later that the entrainment calculations are not sensitive to its value. The comparison between this definition and that based on (4.3) shows that they are only close over a small portion of the OF height with large deviations at the top and bottom of the flow height. The source of this difference can be found in figure 10. The ambient fluid is not quiescent above z_m but has a velocity profile that extends into the domain a long distance after $\overline{\phi} \approx 0$, which has the effect of increasing the length scale in (4.3). Additionally, the intrusion affects the flow below $z = 4$ at $Fr = 7$, so the length scale is not expected to apply in this region. The downward flow of the OF and the outward motion of the intrusion along the wall produce a weak circulation cell in the AF. This circulation may also have a small effect on the result.

The inner upflow stream expands rapidly over $z = 0$–2 for $Fr = 4$ and $z = 0$–4 for $Fr = 7$ and then expands very slowly at $\mathrm{d}r/\mathrm{d}z \approx 0.03$ over $z = 2$–6 for $Fr = 4$ and $\mathrm{d}r/\mathrm{d}z \approx 0.04$ over $z = 4$–9.5 for $Fr = 7$, as shown in figure 12. The maximum velocity in the OF is located at $r \approx 2.5$ and $r \approx 3.0$, largely independent of z, for $Fr = 4$ and $Fr = 7$, respectively. The IF contracts after $z \approx 7$ and $z \approx 11.5$ for $Fr = 4$ and $Fr = 7$, respectively. The downflow expands at the base of the fountain as the plume moves into the intrusion.

It is attractive from a modelling point of view to treat the OF as an independent plume, a flow which is relatively well understood. The integral length scale L_{11} for

https://doi.org/10.1017/S0022112010005872 Published online by Cambridge University Press

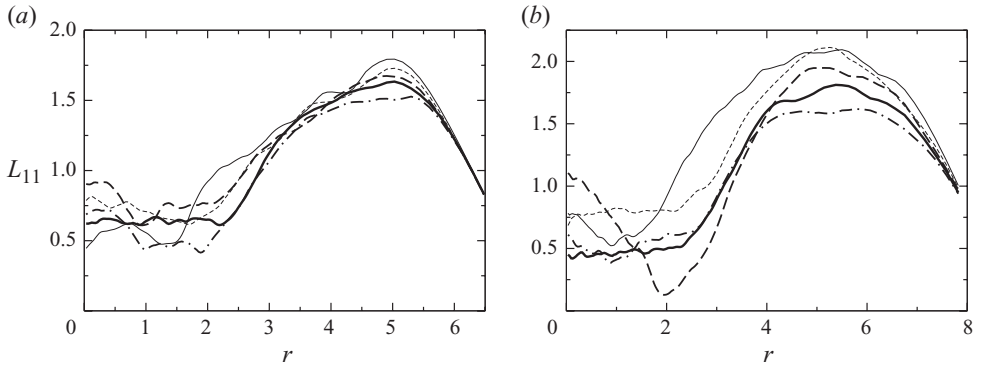


FIGURE 13. L_{11} for $Fr = 4$ (a) and $Fr = 7$ (b). The lines dash-dotted, thick solid, thick dashed, thin dashed, thin solid indicate $z = 3$, $z = 4$, $z = 5$, $z = 6$, $z = 7$ in (a) and $z = 4$, $z = 6$, $z = 8$, $z = 10$, $z = 12$ in (b).

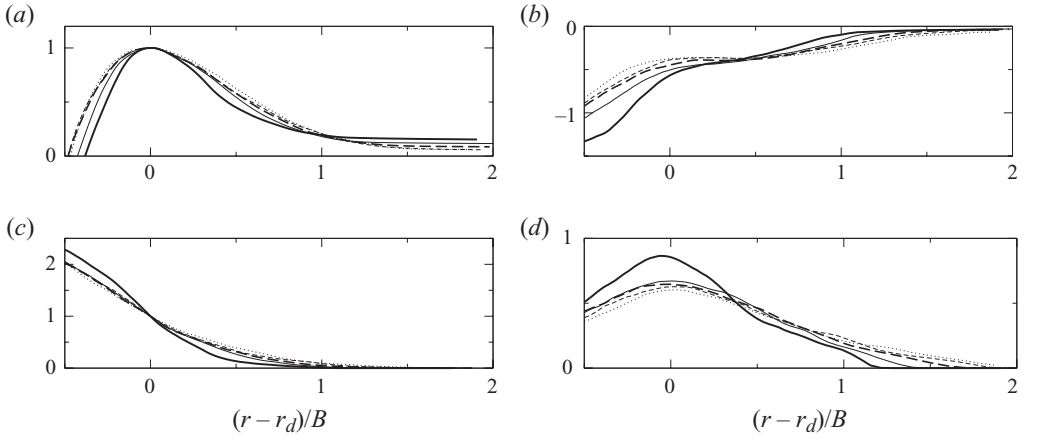


FIGURE 14. Similarity of flow statistics in the OF at $Fr = 7$. (a) $\overline{u_z(r,z)}/\overline{u_z(r_d,z)}$, ($b$) $\overline{u_z'(r,z)u_z'(r,z)}^{0.5}/\overline{u_z(r_d,z)}$, ($c$) $\overline{\phi(r,z)}/\overline{\phi(r_d,z)}$, ($d$) $\overline{\phi'(r,z)\phi'(r,z)}^{0.5}/\overline{\phi(r_d,z)}$. Vertical locations are $z = 5$ – dotted line, $z = 7$ – thin dashed line, $z = 9$ – thick dashed line, $z = 11$ – thin solid line and $z = 13$ – thick solid line.

radial variance $\overline{u_r'(r,z)u_r'(r+s,z)}$ is given as,

$$L_{11}(r,z) = \int_0^{r_{lim}-r} \frac{\overline{u_r'(r,z)u_r'(r+s,z)}}{\sqrt{\overline{u_r'(r,z)^2}}\sqrt{\overline{u_r'(r+s,z)^2}}}\,\mathrm{d}s. \tag{4.4}$$

This result is plotted in figures 13(a) and 13(b) for $Fr = 4$ and $Fr = 7$, respectively. The length scale is relatively flat across the IF region but rises sharply over $r = r_{io} - r_d$. In the OF region over $r = 2.5$–6, the length scale increases to $L_{11} = 2$ for $Fr = 7$ and $L_{11} = 1.7$ for $Fr = 4$, which is approximately half the width of the OF stream. These relatively small length scales suggest the connection between the structures in the IF and the OF is fairly indirect and allows the possibility that the OF may be treated separately. In figure 14, statistics at $Fr = 7$ are normalised by the local flow variable values at $r = r_d$ and the length scale $B_{1/2} + r_d$. Over $z = 5$–11, the curves collapse relatively well suggesting a degree of flow similarity. $\overline{u_r'u_z'}$ and $\overline{u_r}$ (not shown)

https://doi.org/10.1017/S0022112010005872 Published online by Cambridge University Press

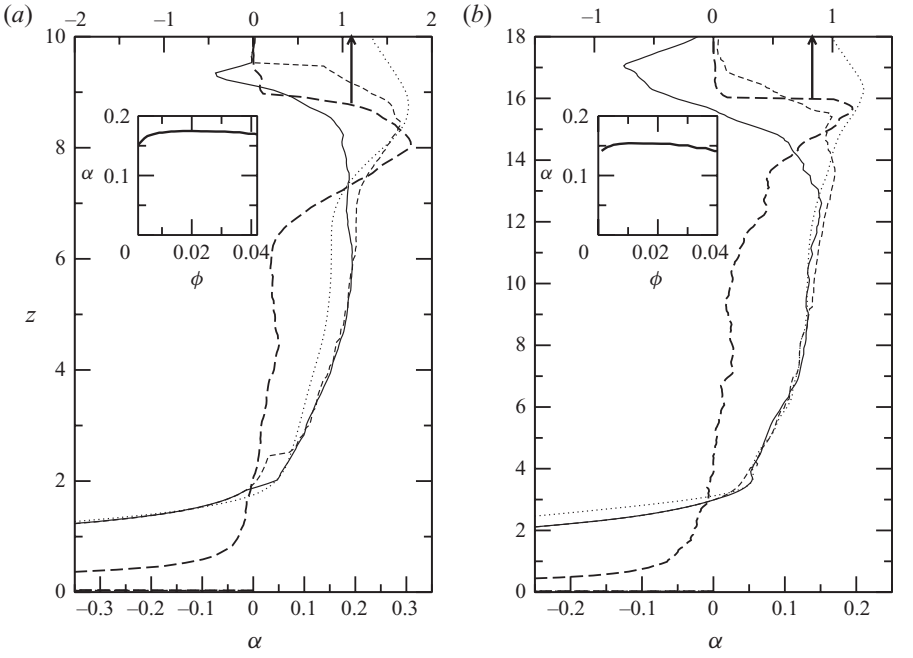


FIGURE 15. Mean entrainment rates for $Fr = 4$ (a) and $Fr = 7$ (b). Entrainment into OF from IF – thick dashed line; entrainment into OF from the AF with the OF/AF boundary r_{oa} defined by the location of $\phi = 0.025$ – solid line, $\phi = 0.005$ – thin dashed line and r_{lim} – dotted line. Inner plot indicates sensitivity of AF entrainment to r_{oa}, as defined by ϕ, at $z = 5$ and $z = 11$ for $Fr = 4$ (a) and $Fr = 7$ (b), respectively.

compare more poorly and are clearly not normalised by $\overline{u_z(r_d, z)}$, possibly because these quantities depend more on the interaction between the IF and OF.

The mean entrainment α between the streams is calculated as

$$\alpha = -s\overline{u_r}/W, \tag{4.5}$$

where $\overline{u_r}$ is obtained at r_{io} for IF/OF entrainment and at r_{oa} for OF/AF entrainment. The entrainment direction is into the OF from both the AF and the IF over most of the height. This direction is taken as positive, so $s = -1$ for the AF/OF boundary and $s = 1$ for the IF/OF boundary. The bulk OF stream velocity is given as

$$W = \frac{b^2W^2}{b^2W}, \tag{4.6}$$

where b^2W^2 and b^2W are defined in (4.1) and (4.2) and $r_1 = 0$ and $r_2 = r_{io}$ for the IF stream and $r_1 = r_{io}$ and $r_2 = r_{oa}$ for the OF stream.

The entrainment rate is plotted in figure 15 for $Fr = 4$ and $Fr = 7$. Results for multiple definitions of r_{oa} are presented and the sensitivity of the entrainment rate to boundary location is also given. The entrainment profile from the AF with $r_{oa} = r_{lim}$ is also shown in figure 15. The entrainment rate is not sensitive to the location of the boundary.

The entrainment profiles illustrate three distinct regions of behaviour. In region 1, over $z = 0$–2 for $Fr = 4$ and $z = 0$–4 for $Fr = 7$, there is entrainment into the IF from the OF. There is entrainment from the OF into the base intrusion or AF over $z = 0$–2 for $Fr = 4$ and $z = 0$–3 for $Fr = 7$. In region 2, for $z \approx 2$–8 for $Fr = 4$ and $z \approx 4$–14 for

https://doi.org/10.1017/S0022112010005872 Published online by Cambridge University Press

$Fr = 7$, there is entrainment from the AF to the OF with $\overline{\alpha} = 0.1$–0.2. Over this region, there is low entrainment into the OF from the IF. In region 3, for $z \approx 8 - z_m$ for $Fr = 4$ and $z \approx 14 - z_m$ for $Fr = 7$, the entrainment regime in both streams is dominated by ejection of fluid from the cap region, so the OF receives fluid from the IF and the AF receives fluid from the OF.

In regions 1 and 3, the flow behaviour shown in figure 15 is unlikely to depend on W and so is not an entrainment mechanism in the same sense as that observed in a plume or jet. In region 2, however, the behaviour may be reasonably well compared to these ubiquitous flows. List (1982) gives the entrainment into a plane buoyant plume as $\alpha = 0.14$ while entrainment into an axisymetric plume has $\alpha = 0.11$. The slightly higher entrainment coefficient found here between the AF and OF may be due to the ambient circulation or the more unsteady pulsing behaviour of the ejection into the OF. The dense fluid enters the OF with higher radial velocity and therefore once it accelerates down, it is able to draw more ambient fluid in behind each pulse than would otherwise occur in a less unsteady flow. This process is illustrated in supplementary movie 3 (available at journals.cambridge.org/flm).

The very low mean entrainment from the IF to the OF in region 2 indicates that most of the mass exchange occurs via $\overline{u_r' u_z'}$ and $\overline{u_r' \phi'}$. Mizushina *et al.* (1982) gives the expansion rate of the IF for higher Froude number flow over $Fr = 15$–70 at $\Delta r_{io}/\Delta z = 0.15$–$0.23$. With a top hat velocity profile, this result indicates $\alpha \approx 0.075$–0.115, with α appearing to decrease with increasing Froude number. These values lie between the typical value for a jet $\alpha = 0.075$ and that for a plume $\alpha = 0.11$. This result then supports the hypothesis that the IF behaves like a jet at very high Froude number and that our result is in a regime where the IF is not fully developed, in agreement with the other observations in § 4.

4.2. *Momentum and mass exchanges*

The vertical flux of volume, momentum, and buoyancy for the IF and OF flow streams, given by

$$Q = 2\int_{r_1}^{r_2} \overline{u_z} r \,\mathrm{d}r, \quad M = 2\int_{r_1}^{r_2} \overline{u_z}^2 r \,\mathrm{d}r, \quad F = 2\int_{r_1}^{r_2} \overline{u_z}\,\overline{\phi} r \,\mathrm{d}r, \tag{4.7}$$

is plotted in figure 16, where $r_1 = 0$ and $r_2 = r_{io}$ for the IF stream and $r_1 = r_{io}$ and $r_2 = r_{lim}$ for the OF stream. At $Fr = 7$, shown in figure 16(b), in the IF, the flux of buoyancy increases over $z = 0$–3 and mass flux increases over $z = 0$–4 with entrainment from the OF. From $z = 5$–12, the IF expands weakly with weak entrainment into the OF. Above $z = 12$, Q in the IF decreases rapidly with radial flow into the OF. In the OF stream, Q increases towards the intrusion, but at $z = z_m$, Q is positive because of the ambient flow. As the flow approaches the intrusion at $z \lesssim 2$, Q, M and F go to zero as u_z goes to zero. A similar behaviour is observed for $Fr = 4$ in figure 16(a). At steady state, the vertical momentum equation is,

$$\left(\frac{\partial\left(r\overline{u_z}^2\right)}{\partial z} + \frac{\partial(r\overline{u_z}\,\overline{u_r})}{\partial r}\right) Fr^2 + r\frac{\partial \overline{p}}{\partial z} Fr^2 - \frac{1}{Re}\left(\frac{\partial}{\partial r}\left(r\frac{\partial \overline{u_z}}{\partial r}\right) + \frac{r\partial^2 \overline{u_z}}{\partial z^2}\right) Fr^2 + \left(\frac{\partial(r\overline{u_z' u_r'})}{\partial r} + \frac{\partial(r\overline{u_z' u_z'})}{\partial z}\right) Fr^2 + \quad r\overline{\phi} = 0. \tag{4.8}$$

In figure 17, the integrated balance terms are given for the IF and OF at $Fr = 7$. The viscous term plotted in the figures is $\int_{R_1}^{R_2} 2V \mathrm{d}r$, where V is the third term in (4.8). This term is shown to be negligible everywhere in both the IF and OF. In the IF,

https://doi.org/10.1017/S0022112010005872 Published online by Cambridge University Press

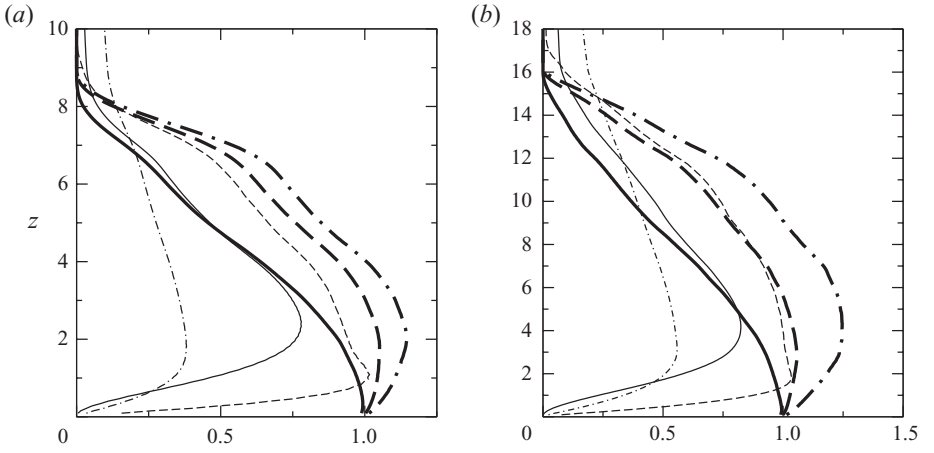


FIGURE 16. Q – dashed-dotted line, M – solid line, F – dashed line for IF stream (thick lines) and $-Q$ – dashed-dotted line, M – solid line, $-0.1F$ – dashed line for OF stream (thin lines) at $Fr = 4$ (a) and $Fr = 7$ (b).

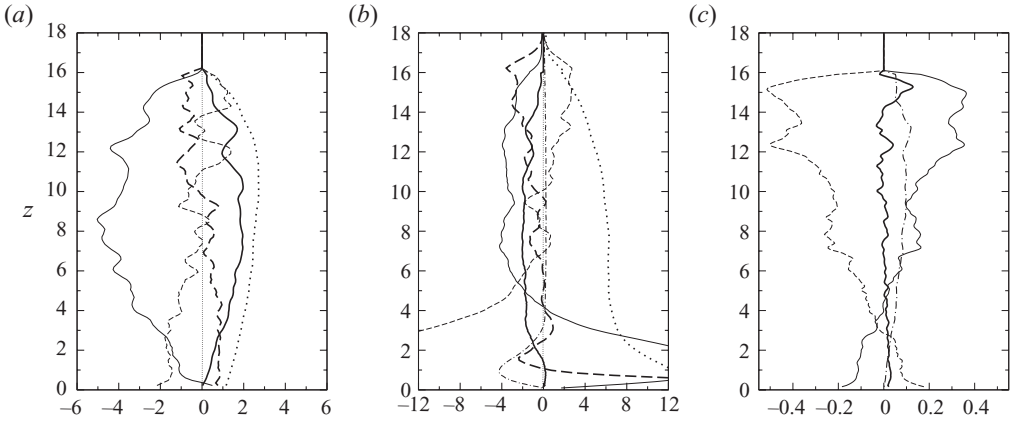


FIGURE 17. Vertical momentum balance of the IF (a) and OF (b) at $Fr = 7$. $\int_{R_1}^{R_2} 2Fr^2 \partial(r\overline{u_z' u_r'})/\partial r \, \mathrm{d}r$ – thick solid line, $\int_{R_1}^{R_2} 2Fr^2 \partial(r\overline{u_z' u_z'})/\partial z \, \mathrm{d}r$ – thick dashed line, $\int_{R_1}^{R_2} 2Fr^2 \partial(r\overline{p})/\partial z \, \mathrm{d}r$ – thin dashed line, $\int_{R_1}^{R_2} 2Fr^2 \partial(r\overline{u_z}^2)/\partial z \, \mathrm{d}r$ – thin solid line, $\int_{R_1}^{R_2} 2Fr^2 \partial(r\overline{u_z}\,\overline{u_r})/\partial r \, \mathrm{d}r$ – thin dash-dotted line and $\int_{R_1}^{R_2} 2(r\overline{\phi}) \, \mathrm{d}r$ – thick dotted line. $\int_{R_1}^{R_2} 2V \mathrm{d}r$ – thin dotted line where V is the viscous term from (4.8). In (c), the vertical scalar transport equation for the IF at $Fr = 7$. $r_{io}(u_r\phi)_{io}$ – thin solid line, $r_{io}(\overline{u_r'\phi'})_{io}$ – dashed-dotted line, $\int_0^{r_{io}} \frac{\partial(ru_z\phi)}{\partial z} \mathrm{d}r$ – dashed line, $\int_0^{r_{io}} \frac{\partial(r\overline{u_z'\phi'})}{\partial z} \mathrm{d}r$ – thick solid line.

illustrated in figure 17(a), from $z = 0$ to 4, there is a strong axial pressure gradient caused by the axial deceleration of the OF where it meets the lower bounding wall and its subsequent radial acceleration outwards in the intrusion. A similar behaviour was observed in weak fountain flow by Williamson *et al.* (2010). The other terms in the balance are also significant in this region as the shear layer rapidly forms around the IF. From $z = 4$ to 7, the pressure gradient decreases. From $z \approx 7$ to 10, the balance is approximately

$$\int_0^{r_{io}} 2(r\overline{\phi}) \, \mathrm{d}r + 2Fr^2 r_{io} \left(\overline{u_z' u_r'}\right)_{io} \approx -\int_0^{r_{io}} 2Fr^2 \frac{\partial\left(r\overline{u_z}^2\right)}{\partial z} \, \mathrm{d}r. \tag{4.9}$$

https://doi.org/10.1017/S0022112010005872 Published online by Cambridge University Press

The behaviour assumed in integral models follows (4.9) but with the added term $2Fr^2 r_{io}(\overline{u'_z u'_r})_{io}$ accounting for the effect of the downflow (Morton, Taylor & Turner 1956; Abraham 1967; Bloomfield & Kerr 1998; Kaye & Hunt 2006). In the attempts to produce an analytical model, this extra term is neglected with the assumption that the OF is either having a very weak effect on the IF, or is only attempting to model the initial transient stage before the OF has formed. At $Fr = 7$, the diffusion term is only slightly smaller than the buoyancy term in magnitude in this region, and hence cannot be neglected.

After the shear layer merges at $z \approx 10$, $\overline{u'_z u'_z}$ reaches its maximum value and the term $\int_{R_1}^{R_2} 2Fr^2 \partial(r\overline{u'_z u'_z})/\partial z \, \mathrm{d}r$ becomes negative. This term is also typically neglected in integral models of jets and plumes (e.g. Morton 1959) but becomes an increasingly significant proportion of the momentum transfer towards the top of the fountain flow simulated here.

The dynamics at the top of the fountain, illustrated in figures 4 and 5, show that the pressure gradient is important, with a high-pressure region close to z_m and a surrounding low-pressure region in the adjacent OF. This is reflected in the momentum balance in figure 17(a) over $z = 10 - z_m$. The top of the fountain is a complex balance between all the terms. Buoyancy and pressure oppose the advection and diffusion of momentum vertically.

In the OF, shown in figure 17(b), over $z = 0$–4, the momentum balance is dominated by the intrusion. Over $z = 5$–12, the pressure gradient is small and the balance is similar to that in (4.9), but $r_{io}(\overline{u'_z u'_r})_{io}$ acts in the opposite direction and unlike a line plume is significant. In the cap region over $z = 12 - z_m$,

$$\int_{r_{io}}^{r_{lim}} 2(r\overline{\phi}) \, \mathrm{d}r + \int_{r_{io}}^{r_{lim}} 2Fr^2 \frac{\partial(r\overline{p})}{\partial z} \, \mathrm{d}r \approx \int_{r_{oi}}^{r_{lim}} 2Fr^2 \frac{\partial\left(r\overline{u'_z u'_z}\right)}{\partial z} \, \mathrm{d}r - \int_{r_{io}}^{r_{lim}} 2Fr^2 \frac{\partial\left(r\overline{u}_z^2\right)}{\partial z} \, \mathrm{d}r, \tag{4.10}$$

so the pressure gradient and buoyancy work against $\int_{r_{oi}}^{r_{lim}} 2Fr^2 \partial(r\overline{u'_z u'_z})/\partial z \, \mathrm{d}r$. In figure 17($c$), the balance terms for the scalar transport equation are given for the IF. This balance illustrates that over $z = 0$–4, there is mean flow entrainment of ϕ into the IF at $Fr = 7$. Over $z = 4$–10, $r_{io}(\overline{u}_r\overline{\phi})_{io}$ and $r_{io}(\overline{u'_r\phi'})_{io}$ are approximately equal in transporting ϕ outwards into the OF. Over $z = 10 - z_m$, $r_{io}(\overline{u}_r\overline{\phi})_{io}$ is more significant.

5. Effect of a turbulent inlet condition

Williamson *et al.* (2010) found that at very weak Froude numbers, source turbulence and velocity profile have a minimal effect on flow behaviour as the flow is driven entirely by a hydrostatic balance. For weak flow at $Fr = 1$, the source velocity profile was found to be important for prediction of fountain height. In the present work, we test the effect that source turbulence and velocity profile have on important flow quantities by performing an additional simulation of the $Fr = 7$ flow with an unsteady inlet condition derived from a separate turbulent pipe flow simulation. This technique was used by Williamson *et al.* (2010) and the reader is referred to that work for full details. The momentum at the source is higher in the pipe flow result owing to the velocity profile, but the initial inlet flow rate Q is identical. The reduced gravity σ is greater for the pipe flow simulation to give the same effective Froude number. The simulations were run in the same manner as the laminar source simulations and flow statistics were recorded for $\Delta t = 120$ after steady-state behaviour was obtained. The results are compared with the laminar source results in figures 18 and 19.

https://doi.org/10.1017/S0022112010005872 Published online by Cambridge University Press

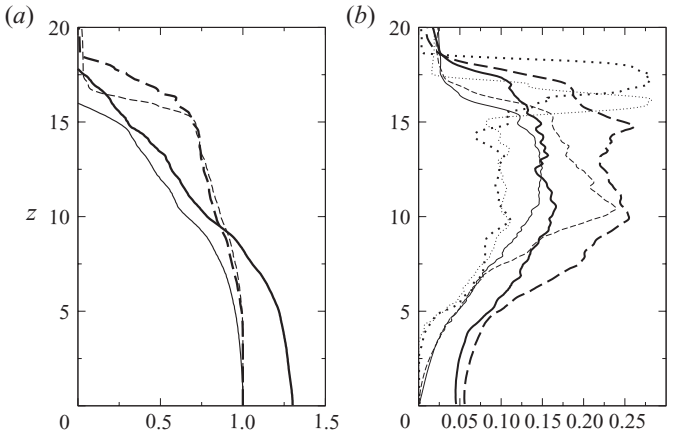


FIGURE 18. Mean flow profiles of $\overline{u_z}$ – solid line, $\overline{\phi}$ – dashed line all interpolated onto $r=0$ at $Fr=7$ (a). In (b), $\overline{u_z'u_z'}^{0.5}$ – dashed line, $\overline{u_r'u_r'}^{0.5}$ – solid line, $\overline{\phi'\phi'}^{0.5}$ – dotted line. In (a) and (b), thin lines indicate a laminar source and thick lines the pipe flow source.

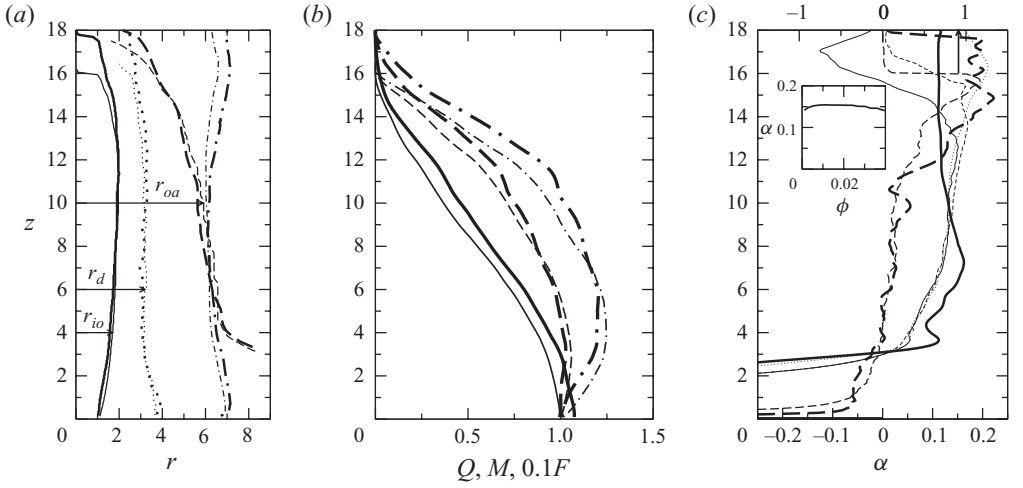


FIGURE 19. Boundaries between flow streams at $Fr=7$ (a) with line definitions given in figure 12. In (b), Q – dashed-dotted line, M – solid line and $0.1F$ – dashed line are plotted for the IF. In (c), the entrainment between the flow streams is indicated with definitions given in figure 15. In (a)–(c), thin lines indicate a laminar source and thick lines the pipe flow source.

In figure 18(a), $\overline{u_z}$ is plotted along the fountain axis together with $\overline{\phi}$. The centreline velocity in the pipe flow is initially higher but has the same development behaviour as the laminar result with the velocity decreasing nonlinearly over $z=0$–9 and then decreasing linearly over 9–15. Over $15-z_m$, the laminar result decreases more rapidly than the pipe flow result. The profile of $\overline{\phi}$ is similar with both inlet conditions but with increased height in the pipe flow simulation. The second-order statistics are shown in figure 18(b). With the pipe flow result, the incoming stresses are advected into the domain from the turbulent inlet condition. The peak in $\overline{u_z'u_z'}^{0.5}$ occurs in the same place with both inlet conditions, being where the shear layer merges. $\overline{\phi'\phi'}^{0.5}$ has nearly identical behaviour with the two inlet conditions as does $\overline{u_r'u_r'}^{0.5}$, apart from the difference in height.

https://doi.org/10.1017/S0022112010005872 Published online by Cambridge University Press

The boundaries between the flow streams are given in figure 19(*a*). The OF definition and the location of r_d are nearly identical in both the simulations. In the IF, the laminar uniform source simulation expands slightly more rapidly for $z < 3$ but is nearly identical to the turbulent pipe flow results from $z = 3$ to 14. From $z = 14$ to 16, the IF for the laminar source simulation contracts while in the pipe flow result the IF is taller, ending at $z = 17.8$. In figure 19(*b*), the IF M, Q and F are plotted. The OF comparison is very close and hence is not presented here. Q increases more rapidly over the initial $z = 0$–4 expansion region with the laminar source, thus entraining fluid more rapidly. The plots of M and F are similar with the two inlet conditions. The entrainment profile given in figure 19(*c*) indicates that the entrainment coefficients are very similar in the inner flow except near the top of the fountain where the increased height results in a mismatch between the results. In the OF, the entrainment is higher near the top of the fountain in the laminar simulation. In general, this comparison suggests that the turbulent inlet condition has the effect of increasing the fountain height but the OF and development of the IF along the fountain vertical axis are largely the same for both inlet conditions. Similar conclusions may be drawn from the Cresswell & Szczepura (1993) experiments at $Fr = 3.16$. The author found that the stresses advected into the domain from the turbulent pipe flow were significantly lower than the shear stresses generated at the boundary between the IF and OF, suggesting that unlike isothermal jet flow, the inlet turbulence is less significant and fountain flow is dominated by the shear interaction between the IF and OF as has been observed here.

6. Closing remarks

We use the results of this study to clarify previous assumptions regarding the behaviour of fountain flow. Like a non-buoyant jet, the IF has a short developing region with a potential core. Over the first part of this region, fluid is entrained into the IF. The length of the potential core is much shorter at $Fr = 7$ than a non-buoyant jet, ending at $z \approx 10$ with similar observations at $Fr = 4$ and $Fr = 3.1$ (Cresswell & Szczepura 1993). After the shear layer merges from $z = 10$ to 12, $\partial \overline{u_z' u_z'}/\partial z$ becomes negative as happens in the self-similar region of a non-buoyant jet. There is strong mixing between the IF and OF, the dynamics of which are complex. Both $r_{io}(\overline{u_z' u_r'})_{io}$ and $r_{io}(\overline{u_r' \phi'})_{io}$ are very important but it is not clear how these terms depend on vertical location and Froude number. Mean entrainment between the IF and OF is also complex. Results presented by Mizushina *et al.* (1982) suggest that for $Fr > 15$, fluid is entrained into the IF with entrainment rates similar to a non-buoyant jet, while the present work shows that apart from a short developing region near the source, the entrainment is negative in the usual jet sense, i.e. the IF ejects fluid into the OF.

The OF has been compared to a turbulent line plume, with interaction with the IF on the inner boundary and the AF on the outer boundary. Unlike a line plume, there is transfer of momentum from the IF via $r_{io}(\overline{u_z' u_r'})_{io}$, transfer of mass via the mean entrainment mechanism and transfer of the scalar ϕ via $r_{io}(\overline{u_r}\,\overline{\phi})_{io}$ and $r_{io}(\overline{u_r' \phi'})_{io}$. In the outer region, entrainment from the AF is found to be higher than expected in a line plume. Some flow quantities appear self-similar when normalised by variables at the location of maximum downflow velocity. The integral length scales suggest the flow in the outer region, $r \approx B_{1/2} + r_d$, is independent of the IF.

At the top of the fountain in both the IF and OF, there is a cap region where the IF begins to contract ($z \approx 12 - z_m$ at $Fr = 7$) and radial velocity increases. Hunt & Coffey

https://doi.org/10.1017/S0022112010005872 Published online by Cambridge University Press

(2009) suggested that the cap region of a turbulent fountain may be described by the relation for the dynamics of very weak flow given by Kaye & Hunt (2006) where buoyancy force from the fountain height provides the pressure head to accelerate the flow radially. Williamson *et al.* (2010) found evidence for this behaviour in weak fountains over $Fr = 0.4$–2.1. The present results, illustrated in figure 17 and given in the momentum balance in (4.10), show that the energy is extracted from the turbulence via $\partial(r\overline{u_z'u_z'})/\partial z$ which together with the mean flow momentum, balance the pressure gradient and buoyancy term. In this way, the pressure gradient opposes the upflow, unlike at weak Froude numbers, where $Fr^2 \mathrm{d}p/\mathrm{d}z \sim \phi$ (Williamson *et al.* 2010). The opposing pressure may be interpreted as a result of the pulsing in the fountain height forcing the fluid above it out of the way, as illustrated in figure 5. The pressure gradient is produced not from the mean buoyancy field, as in weak fountains, but from the turbulence and acceleration term. This process also has the effect of setting up a radial pressure gradient transporting fluid into the OF. These results suggest that the scaling behaviour for very weak turbulent fountains, $z_m \sim Fr^{2/3}$, does not apply for the cap region of forced fountains.

Both the IF and OF streams have an intrusion-affected region resulting from the lower wall in this flush nozzle configuration. This extends over $z = 0$–2 at $Fr = 4$ and $z = 0$–4 at $Fr = 7$, increasing with Froude number. The scaling for the height of this region clearly has a Froude-number dependence, the exact scaling of which is beyond the scope of this study but may be related to previous work on gravity currents (e.g. Huppert 1982).

The linear Froude number scaling for the fountain penetration height, $z_m \sim Fr$, is a reasonable fit to the fountain penetration heights obtained in this study, but other quantities suggest this is not because of the model behaviour assumed in high-Froude-number flow, as the flow is much more complex than suggested by previous studies. The length scale $z_m \sim M_0^{3/4} F_0^{-1/2}$ obtained by Turner (1966) does not describe the effects of the intrusion region, the behaviour in the cap region or mixing behaviour with the OF. Further investigations are needed at higher Froude number particularly to obtain an understanding of how $r_{io}(\overline{u_z'u_r'})_{io}$, $r_{io}(\overline{u_r'\phi'})_{io}$ and mean entrainment behave at higher Froude number. Since many industrial and geophysical occurrences of these flows are not in the very high-froude-number regime but are in the lower end of the forced regime $Fr \approx 3$–15, further work identifying the nature of the behaviour in this range would be valuable.

The authors acknowledge the support of the Australian Research Council.

Supplementary movies are available at journals.cambridge.org/flm.

REFERENCES

Abraham, G. 1967 Jets with negative buoyancy in homogeneous fluid. *J. Hydaul. Res.* **5**, 235–248.

Baddour, R. E. & Zhang, H. 2009 Density effect on round turbulent hypersaline fountain. *J. Hydraul. Engng* **135**, 57–59.

Baines, W. D., Turner, J. S. & Campbell, I. H. 1990 Turbulent fountains in an open chamber. *J. Fluid Mech.* **212**, 557–592.

Bloomfield, L. J. & Kerr, R. C. 1998 Turbulent fountains in a stratified fluid. *J. Fluid Mech.* **358**, 335–356.

Bloomfield, L. J. & Kerr, R. C. 2000 A theoretical model of a turbulent fountain. *J. Fluid Mech.* **424**, 197–216.

Boguslawski, L. & Popiel, Cz. O. 1979 Flow structure of the free round turbulent jet in the initial region. *J. Fluid Mech.* **90**, 531–539.

https://doi.org/10.1017/S0022112010005872 Published online by Cambridge University Press

Campbell, I. H. & Turner, J. S. 1989 Fountains in magma chambers. *J. Petrol.* **30**, 885–923.

Cresswell, R. W. & Szczepura, R. T. 1993 Experimental investigation into a turbulent jet with negative buoyancy. *Phys. Fluids* A **5**, 2865–2878.

Demetriou, J. D. 1978 Turbulent diffusion of vertical water jets with negative buoyancy (in Greek). PhD thesis, National Technical University of Athens, Department of Civil Engineering.

Hunt, G. R. & Coffey, C. J. 2009 Characterising line fountains. *J. Fluid Mech.* **623**, 317–327.

Huppert, H. E. 1982 The propagation of two-dimensional and axisymmetric viscous gravity currents over a rigid horizontal surface. *J. Fluid Mech.* **121**, 43–58.

Kaminski, E., Tait, S. & Carazzo, G. 2005 Turbulent entrainment in jets with arbitrary buoyancy. *J. Fluid Mech.* **526**, 361–376.

Kaye, N. B. & Hunt, G. R. 2006 Weak fountains. *J. Fluid Mech.* **558**, 319–328.

Leonard, B. P. & Mokhtari, S. 1990 Beyond first-order upwinding: the ultra-sharp alternative for non-oscillatory steady state simulation of convection. *Intl J. Numer. Meth. Engng* **30**, 729–766.

Lin, W. & Armfield, S. W. 2000*a* Direct simulation of weak axisymmetric fountains in a homogeneous fluid. *J. Fluid Mech.* **403**, 67–88.

Lin, W. & Armfield, S. W. 2000*b* Very weak axisymmetric fountains in a homogeneous fluid. *Numer. Heat Transfer* A **38**, 377–396.

Lin, Y. J. P. & Linden, P. F. 2005 The entrainment due to a turbulent fountain at a density interface. *J. Fluid Mech.* **542**, 25–52.

List, E. J. 1982 Turbulent jets and plumes. *Annu. Rev. Fluid Mech.* **14**, 189–212.

Marugán-Cruz, C., Rodríguez-Rodríguez, J. & Martínez-Bazán, C. 2009 Negatively buoyant starting jets. *Phys. Fluids* **21**, 117101.

Mi, J., Nobes, D. S. & Nathan, G. J. 2001 Influence of jet exit conditions on the passive scalar field of an axisymmetric free jet. *J. Fluid Mech.* **432**, 91–125.

Mizushina, T., Ogino, F., Takeuchi, H. & Ikawa, H. 1982 An experimental study of vertical turbulent jet with negative buoyancy. *Wärme-und Stoffübertragung* **16**, 15–21.

Morton, B. R. 1959 Forced plumes. *J. Fluid Mech.* **5**, 151–163.

Morton, B. R., Taylor, G. I. & Turner, J. S. 1956 Turbulent gravitational convection from maintained and instantaneous sources. *Proc. R. Soc. Lond.* **234**, 1–23.

Pantzlaff, L. & Lueptow, R. M. 1999 Transient positively and negatively buoyant turbulent round jets. *Exp. Fluids* **27**, 117–125.

Papanicolaou, P. N. & Kokkalis, T. J. 2008 Vertical buoyancy preserving and non-preserving fountains, in a homogeneous calm ambient. *Intl J. Heat Mass Transfer* **51**, 4109–4120.

Sendan, R. A., Behnia, M. M. & Abreu, K. E. 1978 Temperatures in a heated air jet discharged downward. *Intl J. Heat Mass Transfer* **21**, 1453–1458.

Suzuki, Y. J., Koyaguchi, T., Oqawa, M. & Hachisu, I. 2005 A numerical study of turbulent mixing in eruption clouds using a three-dimensional fluid dynamics model. *J. Geophys. Res.* **110**, B08201.

Turner, J. S. 1966 Jets and plumes with negative or reversing buoyancy. *J. Fluid Mech.* **26**, 779–792.

Williamson, N., Armfield, S. W. & Lin, W. 2008*a* Direct numerical simulation of turbulent intermediate Froude number fountain flow. *ANZIAM J.* **50**, C16–C30.

Williamson, N., Armfield, S. W. & Lin, W. 2010 Transition behaviour of weak turbulent fountains. *J. Fluid Mech.* **655**, 306–326.

Williamson, N., Srinarayana, N., Armfield, S. W., McBain, G. D. & Lin, W. 2008*b* Low-Reynolds-number fountain behaviour. *J. Fluid Mech.* **608**, 297–317.

Zhang, H. & Baddour, R. E. 1997 Maximum vertical penetration of plane turbulent negatively buoyant jets. *J. Engng Mech.* **123**, 973–977.

Zhang, H. & Baddour, R. E. 1998 Maximum penetration of vertical round dense jets at small and large Froude numbers. *J. Hydraul. Engng* **124**, 550–553.

https://doi.org/10.1017/S0022112010005872 Published online by Cambridge University Press